Investigating the Fabrication of Perovskite Solar Cells by Ultrasonic Spray Coating: A Design of Experiments Approach

Peer-reviewed author version

SILVANO, Joao; HAMTAEI, Sarallah; VERDING, Pieter; VERMANG, Bart & DEFERME, Wim (2023) Investigating the Fabrication of Perovskite Solar Cells by Ultrasonic Spray Coating: A Design of Experiments Approach. In: ACS Applied Energy Materials, 6 (14) , p. 7363 -7376.

DOI: 10.1021/acsaem.3c00491
Handle: http://hdl.handle.net/1942/40655

Investigating the Fabrication of Perovskite Solar Cells by Ultrasonic Spray Coating: A Design of Experiments Approach

Joao Silvano*[123], Sarallah Hamtaei[123], Pieter Verding[12], Bart Vermang[123], Wim Deferme[12].

1. Imec − Partner in Solliance, Kapeldreef 75, 3000 Leuven, Belgium;
2. Hasselt University, Institute for Materials Research, Wetenschapspark 1, 3590 Diepenbeek, Belgium;
3. EnergyVille, Thor Park 8320, 3600 Genk, Belgium.

*joao.silvano@uhasselt.be

1. Abstract

The incrementally rising efficiency of perovskite-based photovoltaic devices has established the technology as a hot topic in the past years. Transitioning this class of materials from laboratorial to commercial application is key for the future of clean energy generation. In the interest of this transition, scalable fabrication and reproducibility are challenges to be overcome. Additionally, being a highly dynamic field with fast passed innovation, perovskite research lacks in structured comprehensive studies focusing on the processing parameters, especially when compared to commercial technologies, such as Silicon-based devices. This study proposes a design of experiment (DoE) approach to analyse and optimize the fabrication of perovskite thin films by ultrasonic spray coating, a scalable technique. The inspection of deposition parameters one factor at a time (OFAT) and the more in-depth full factorial analysis of three key input variables allowed the assessment of the impact level of each factor on the obtained films quality and performance of the fabricated photovoltaic devices. Furthermore, the full factorial analysis reveals the presence of interactions between factors. The study revealed that a shorter distance between air gun and sample (2 cm), coupled with high gas pressure (7.6 bar) during the quenching step were the most influential parameters for the production of high-quality films, leading to an average efficiency of 14.8%.

Key Words: Perovskite, Solar Cell, Design of Experiment, Scalable, Photovoltaics

2. Introduction

The continuous worldwide trend towards reduced emissions of greenhouse-gases, amplified by the current political crisis bringing instability to the energy sector worldwide [1], has led investors to pay more attention than ever to alternative clean energy generation [2], such as wind and solar power. Thin film photovoltaic technologies have long been seen as a possible way of boosting solar power generation by reducing the material costs related to solar panel manufacturing, with tandem devices further maximizing the efficiency of these installations. Owing to its incrementally rising efficiencies [3], low processing temperature [4], and flexible composition allowing for band gap tunability [5], perovskite solar cells (PSC) are highly compatible with tandem application and are therefore in the forefront of photovoltaic research in recent years.
Despite exhibiting efficiencies over 25% [6], stability is still a major obstacle on the road to industrialization and commercialization. Degradation due to oxygen, humidity, heat, and light [7] results in a high dependency of controlled environment during fabrication of perovskite films, which in turn introduces replicability difficulties from one laboratory to another. Additionally, the employment of manual processing techniques, with the most used deposition method being spin coating, contributes to these replicability problems. While simple and capable of producing homogeneous films on a laboratory-scale, spin coating is a batch process with limited scalability and reproducibility. Automated and large-area-

compatible deposition methods, such as ultrasonic spray coating (USSC) [8, 9, 10, 11], inkjet printing, and blade coating, offer an avenue for upscaling PSC production. Yet, process optimization is still required before matching the solar cell performances of devices fabricated by spin coating [12, 13].

Design of experiments (DoE) is a systematic method which allows the study and optimization of processes by analyzing the relationship between input variables and output responses in a structured manner. This approach has long been used by Silicon-based industry, and more recently had its benefits demonstrated in thin film photovoltaics research [14, 15]. Being a relatively newer material in photovoltaic application, perovskite fabrication is often studied by trial-and-error approaches, with DoE analyses focusing on understanding the properties of perovskite crystals [16], instead of their application in thin film photovoltaics - or focused on the hole transport layer (HTL) of such devices [17]. A similar observation can be made for ultrasonic spray coating as a deposition method, which is often optimized by trial-and-error, with most reporting being limited to the experimental section of articles describing only the best-found parameters.

Examples of DoE are one factor at a time (OFAT) and full factorial analyses. The OFAT approach studies each variable individually and can be used to quickly understand their influence on a response parameter. It is indicated to study a large set of variables quickly, however it might miss an optimal point located outside of the studied range. Full factorial analysis permits the simultaneous analysis of multiple variables and can be used to inspect the entire range of a process. It provides a more comprehensive visualization of the process, at the cost of time and increased complexity.

This study proposes a DoE approach as a proof-of-concept for the optimization of the fabrication of perovskite thin films for photovoltaic devices. The generation of a complete set of data covering all parameters of the fabrication and subsequent modelling are not in the scope of this study.

Initially the entire process is reviewed (**Figure 1**), from substrate cleaning and solution preparation to deposition and post treatment of the film, and process variables are defined. Based on this analysis and previous findings [18], the variables are evaluated, and experiments are designed. The target of the experiments is to gain further insight on two key steps of the process: the deposition of a wet layer of precursor solution by ultrasonic spray coating, and the gas-quenching of the solvent for perovskite crystallization.

The deposition step is examined by a one factor at a time approach, with the establishment of a set of standard parameters followed by the variation and analysis of each parameter effect individually. Then, the gas quenching-assisted evaporation is thoroughly studied by a full factorial analysis of three variables that influence the evaporation rate of the solvent: gas (nitrogen, N_2) pressure, distance between nitrogen gun and substrate, and solvent volatility, or the ratio between a low volatile and a high volatile solvent, which is often a considered factor for controlling the quality of crystalline perovskite films [19, 20, 21]. The produced films are then characterized regarding their morphology and performance as the active layer of a solar cell.

By employing design of experiments principles, it is possible to verify the importance of the ultrasonic spray coating parameters during deposition of a precursor solution for the realization of a uniform wet layer. Moreover, the full factorial analysis reveals an even greater impact of the studied parameters on the quality of the obtained perovskite film, as well as on its performance as the active layer of a solar cell. High gas pressure and the low distance between the nitrogen gun and the substrate come forward as the most influential factors in the obtainment of compact crystalline films. These parameters result in the fabrication of solar cells with open circuit potentials above 900 mV, leading to power conversion efficiencies (PCE) of more than 14%.

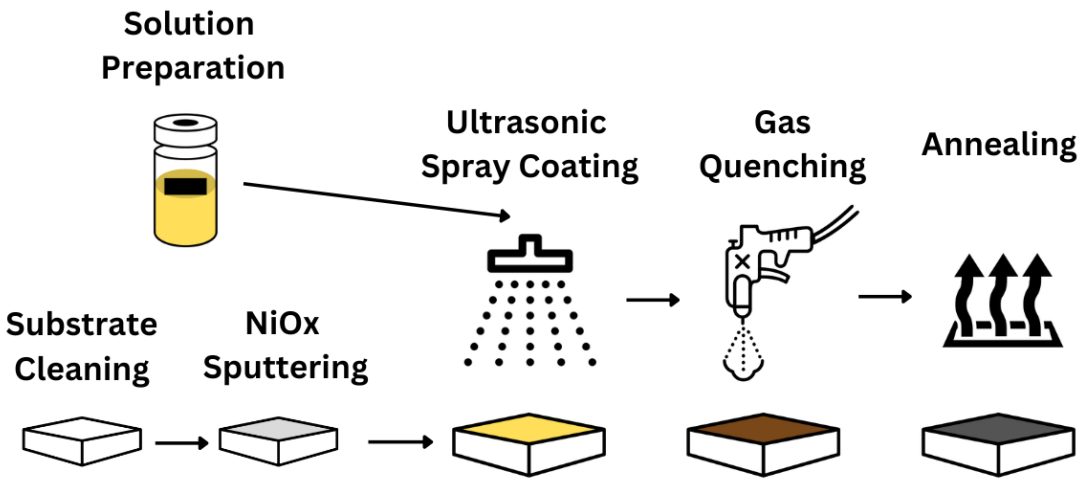

Figure 1: Overview of the fabrication process of perovskite films by ultrasonic spray coating, from substrate preparation to post treatment of the deposited film.

3. Experimental Section and Methodology

The experiments conducted in this study are centered around the fabrication and characterization of perovskite thin layers and perovskite solar cells. For this, two types of samples are produced, with the only difference being the presence or absence of a triple electron transport layer (ETL) and top electrode as described in the device fabrication section below. Samples without the top layers are used for morphology analysis, while the complete solar cells have their performance assessed.

3.1. Solution Preparation

The desired perovskite composition is $Cs_{0.18}FA_{0.82}Pb(I_{0.94}Br_{0.06})_3$. This is chosen due to its bandgap of 1.6 eV, as demonstrated in a previous study [18], which is ideal for monolithic tandem application with a CIS bottom cell (1.0 eV) [22]. This composition is achieved by preparing precursor solutions with the powders mixed following stochiometric proportions. Lead(II) iodide (PbI2) (from TCI), formamidinium iodide (FAI) (from DYESOL) and caesium bromide (CsBr) (from abcr) are diluted in a mixture of Dimethylformamide (DMF) and N-Methyl-2-Pyrrolidone (NMP) (both from Sigma Aldrich), with a final concentration of 0.8 M (considering the perovskite formula). The proportion of NMP to DMF is one of the variables of interest in this study, ranging from 10 to 20% NMP (of the total volume), corresponding to the half and the total concentration used in inks for spin coating deposition, respectively. All solutions are stirred for a minimum of 24h before use. The powders are weighted in a dry room with controlled low humidity, and the solution is prepared inside a N_2-filled glove box.

3.2. Substrate Cleaning

The substrates used are 3x3 cm glass slides coated with two 150 nm thick stripes of Indium-Tin-Oxide (ITO) (from Colorado Concept). Prior to any deposition, the ITO-coated glass is standardly cleaned by immersion in sequential ultrasonic baths in the presence of soap solution, water, acetone, and isopropyl alcohol (IPA), for 30, 15, 10, and 10 minutes, respectively. The substrates are then dried with a N_2 gun and go through a final cleaning step of UV-Ozone exposure for 15 min.

3.3. Device Fabrication

The solar cells follow a p-i-n architecture and are produced by sequential layer depositions on the ITO coated glass substrates. A 15 nm thick nickel oxide (NiOx) hole transport layer (HTL) is deposited by sputtering from a nickel metallic target under O_2 plasma using a Nebula linear sputtering system (from Angstrom Engineering Inc.) and subsequently annealed in air at 300 °C for 20 min after temperature ramp-up. After this, the samples are transferred to a N_2-filled glovebox for the deposition of the perovskite active layer, after which contact with air is limited to a minimum. The previously described precursor solution is deposited on top of the NiOx layer with an ultrasonic spray coater (from Sono-Tek) equipped with an Impact nozzle (Sono-Tek), in which the ultrasonicated mist is projected to the substrate by an auxiliary N_2 flow. During the deposition the substrate is kept on top of a hotplate with adjustable temperature. Gas quenching is performed immediately after the deposition of the precursor ink by applying a N_2 flow (via air gun) orthogonally to the wet film. The air gun used is attached to a N_2 line with maximum pressure of 7.6 bar. The quenched perovskite films are annealed at 100 °C for 30 min to eliminate remaining solvent and promote grain growth.
In the case of the solar cells, the process is continued with the deposition of the ETL and metallic electrode by thermal evaporation (deposition tools from Angstrom Engineering Inc.). The ETL is a triple layer of 1 nm lithium fluoride (LiF), 15 nm buckminsterfullerene (C60) (from Nano-C) and 5 nm bathocuproine (BCP) (from Lumtech). The metallic electrode is a 100 nm layer of copper (Cu) deposited after mechanical etching to partially expose the edges of the ITO stripes. The patterned copper is deposited with the aid of a 16 rectangles mask, in which 4 of those (deposited over the exposed ITO) function as the bottom contact, while the rest function as top contacts. The areas where copper overlaps with the patterned ITO give origin to 12 cells of 0.125 cm2 active area. The final layer architecture of the cell is as follows: Cu/ITO/NiOx/Perovskite/LiF/C60/BCP/Cu. **Figure 2** shows a representation of a sample with 12 cells.

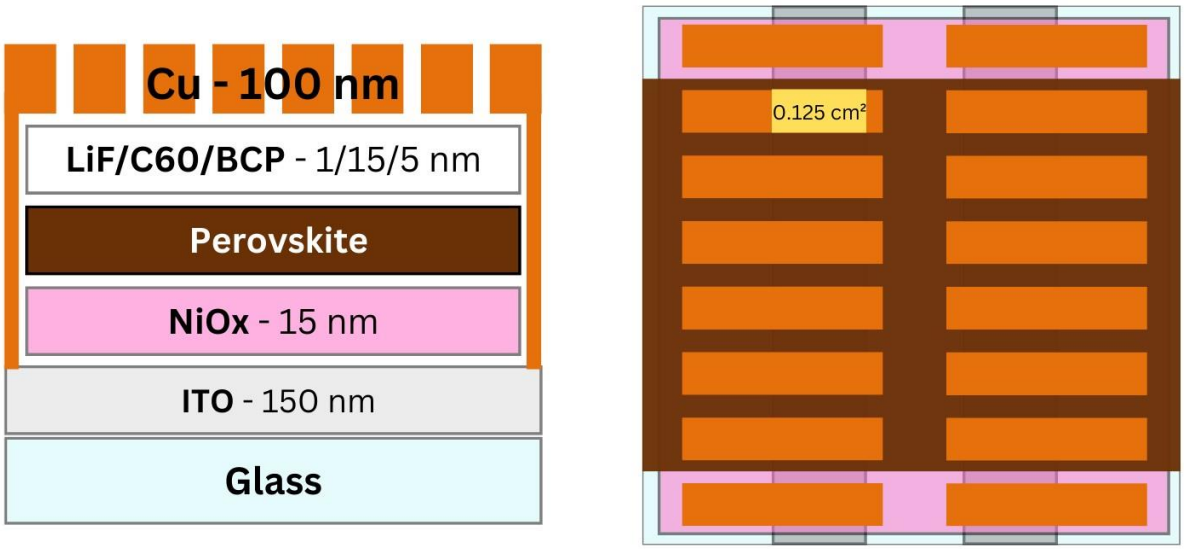

Figure 2: Representation of the layer architecture of a sample with 12 solar cells. The area of one cell, highlighted in yellow, corresponds to the intersection between a top Cu electrode and the bottom ITO stripe.

3.4. Characterization and Software Analysis

Scanning electron microscopy (SEM) analysis is performed with a FEI Quanta 200 FEG-SEM. Optical microscopy imaging is performed with a KEYENCE VK-X 250 3D laser

scanning confocal microscope. The performance of solar cells is determined by current-voltage (IV) measurements using a solar simulator with a Xe arc lamp light source (from Abet technology), under one sun AM 1.5G irradiation, and with a Keithley 2602A source meter. This performance characterization is performed in a controlled environment (N2-filled glove box). A cooling fan is used to maintain the cells at room temperature during measurements. External quantum efficiency (EQE), reflection, and transmission measurements are performed with a Bentham PVE300 spectral response setup with halogen and Xenon lamps. The statistical analysis and modelling based on collected data are performed in JMP® (SAS institute Inc.) software. Grain size determination is performed on an internal software.

3.5. Process Overview

The first step in design of experiments is doing a comprehensive overview of the process to be studied, considering any parameters that may influence the outcome of the process. For this study, the borders of the process start with substrate and solution preparation and finish with the annealing of the perovskite film. The synthesis or production of purchased chemicals or materials is not considered. The deposition of layers other than the active perovskite layer is kept constant and performed by automated processes, such as linear sputtering and thermal evaporation. Moreover, factors related to the environment where the process takes place, such as humidity, presence of contaminants, and temperature are highly important in the processing of perovskite, but will not be considered as variables since all processes are performed in the best environment available within our facilities, as described previously in the experimental section.

3.5.1. Substrate Cleaning

To eliminate impurities and guarantee substrates will be standardized, thorough cleaning is performed before use. Immersion in ultrasonic bath is the method of choice due to the uniformity across batches. With such method, one can use different liquids and solvents in different orders, control the time of each step, as well as temperature. The final drying of substrates is an important step, as it should be done uniformly and quickly, to avoid drying marks. The presence or absence of the UV-Ozone treatment, as well as time of exposure to it can also influence the wettability of the substrate.

Variables: Solvents used; Order of solvents; Time in ultrasonic bath; Temperature during ultrasonic bath; Drying method; Presence of UV-Ozone treatment; Time of UV-Ozone treatment.

3.5.2. Solution Preparation

Ink preparation is an important step in any fabrication involving solution processing. Limiting exposure to air and humidity and precise portioning of powders are vital for obtaining the desired final perovskite composition on the crystalline film. The presence of additives, such as MACl [23], can also lead to increased cell performance, and the selection of solvent (or mixture of solvents) greatly influences the evaporation rate during crystallization.

Variables: Solvents used; Ratio of solvents; Final concentration; Mixing time; Perovskite composition (includes salts used and their proportion); Presence of additives; Quantity of additives.

3.5.3. Ultrasonic Spray Coating

Before the ultrasonic spray coating of the perovskite layer, a NiOx hole transport layer is deposited on the clean ITO-patterned glass. The deposition of this layer is kept constant in all experiments, since it has been optimized and reported before [24, 25].
The Sono-Tek spray coater is equipped with a hotplate and a mechanical arm, allowing for movement on the X, Y, and Z axes.The nozzle is connected to a programable syringe pump. In this way, most parameters can be controlled and automized with high precision via software and/or the equipment panel. The software can be used to program the mechanical arm with a routine, including the speed of movement, position, and repetition cycles. In addition, it controls when the nozzle will be spraying during this routine. The flow rate of ink is determined in the syringe pump settings. The Impact nozzle, mounted on the mechanical arm, operates with an auxiliary N_2 gas flow. The combination of the horizontal flow from the nozzle with the vertical N_2 flow results in a wide spray, ideal to coat large areas. The N_2 flow can be adjusted by a built-in valve.

Variables: Temperature (hotplate); Number of passes; Path Speed; Position of the sample in relation to the spray (including nozzle height, spray angle, and XY position); Flow rate of precursor solution; N_2 pressure (auxiliary gas).

3.5.4. Gas Quenching

With a wet layer of precursor solution deposited on the substrate, it becomes crucial to control the speed in which solvent is eliminated. This will influence important steps in the crystallization of perovskite. Many techniques have been proposed for assisting rapid solvent evaporation, a step typically referred to as :quenching". Anti-solvent quenching can produce high quality films [26] but has scalability limitations. Gas quenching is a simple alternative with high scalability [11, 27] and is therefore selected for this study. Other noteworthy techniques are flash infrared annealing [28], and plasma quenching [29].
For the gas quenching step, the pressure on the N_2 line can be regulated with an external valve, reaching a maximum of 7.6 bar when fully open. A mobile air gun connected to the line allows the quenching step to be performed inside the spray coater glovebox, immediately after deposition of the solution.

Variables: Time under N_2 flow; N_2 pressure; Distance between air gun and sample.

3.5.5. Annealing

The quenched samples are annealed in a hotplate to eliminate any remaining solvent and promote grain growth. The same hotplate built in the spray coating system is used for this step to limit exposure to air and sample handling to a minimum. The temperature is regulated with a PID controller.

Variables: Annealing time; Annealing temperature (hotplate temperature).

3.6. Selection of Variables and Design of Experiments

After the process overview above, an evaluation of variables is drawn considering their expected impact in the quality of the crystalline perovskite layer and solar cell performance. This evaluation in based on previous experience of the research group, as well as observations reported in literature, while considering the focus on scalability of the process proposed in this study.
Although necessary for the process, the substrate cleaning step is believed to be mostly optimized. The ultrasonic cleaning technique involving a variety of solvents has been used for many years in a multitude of applications. Hence, studying the variables in this step is less necessary.

The solution preparation can have a major impact on the obtained perovskite film. The choice of salts and their proportion define the final perovskite composition, which can be useful for added functionalities, such as 2D passivation layers [30] or tunning of the material bandgap [31]. With a focus on upscaling, this study refrains from analysing multiple perovskite compositions, which often require a complete re-optimization of the process conditions; Hence a particular stoichiometry is selected as described previously. On the other hand, controlling the evaporation rate during the quenched-assisted crystallization step is of great interest. One way of doing so is by manipulating the volatility of the solvent mixture, tunning the proportion of solvents in a binary mixture - one with a higher boiling point (NMP) and one with a lower boiling point (DMF).
Ultrasonic spray coating is the method of choice for the deposition of a homogeneous fully covering wet layer of precursor solution. Without an uniform deposition, no crystalline perovskite can be obtained. Hence, all parameters in this step of the process must be considered. Similarly, the quenching step has great impact on the crystallization of perovskite. The gas pressure and the distance between air gun and substrate directly influence how much the directed gas will interact with the wet layer, and how it will lead to solvent evaporation. The duration of the quenching step can be visualized by the typical color change on the layers, from the bright yellow of the precursor solution to the dark brown of the crystalline perovskite film. Additional time under N_2 flow after the quenching is completed does not cause any major change on the film.
Finally, the annealing step serves as a final removal of solvent and can promote grain growth. The optimization of annealing temperature and time can greatly improve solar cell efficiency and stability [31]. The process of optimization of annealing time and temperature is extensively described in literature for a multitude of perovskite compositions [32, 33], therefore we use a constant annealing procedure, subjecting the quenched samples to a hotplate at 100°C for 30 min.
With these considerations, two separate studies are formulated (**Figure 3**). The first is an OFAT analysis on the ultrasonic spray coating parameters (namely hotplate temperature, number of passes, path speed, position of the sample, ink flow rate, and N_2 pressure). The interest of this study is on how each parameter influences the deposition of the precursor ink, and the effect this has on the resulting perovskite solar cells. The second study is a full factorial analysis of three variables believed to highly influence the solvent evaporation during quenching: distance between the air gun and the film, gas pressure, and solvent volatility - here studied as the volumetric percentage of NMP in the total solvent mixture of NMP and DMF. For this full factorial study, not only the performance of resulting cells is assessed, but also the morphology of the resulting perovskite films (thickness and grain size).

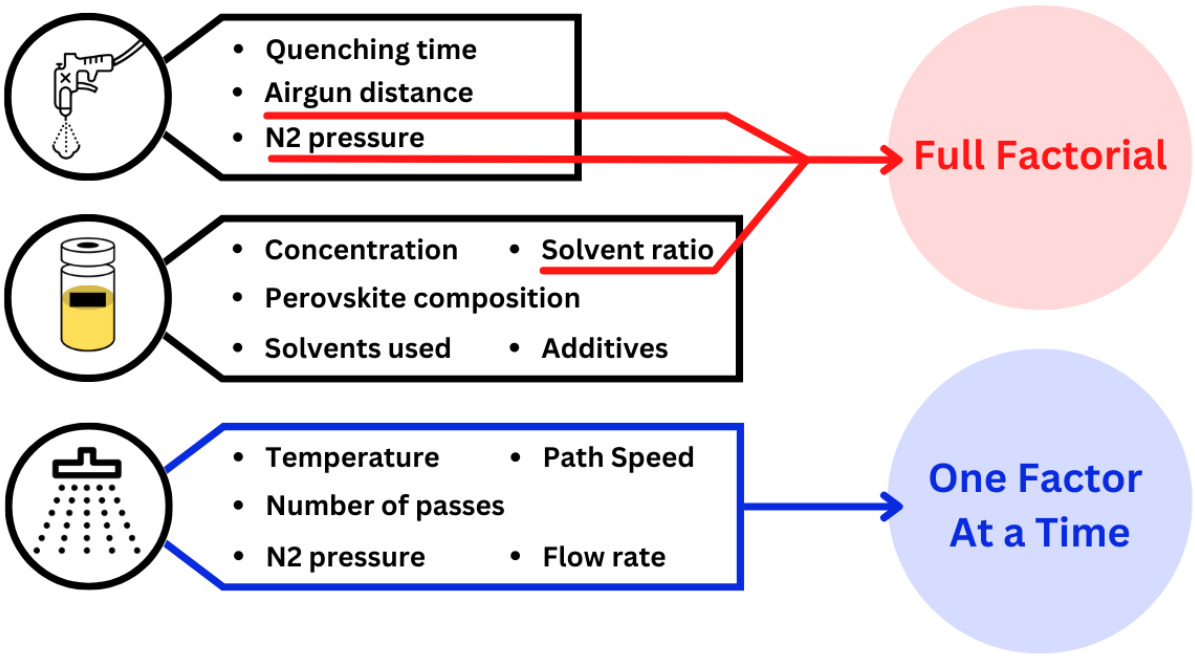

Figure 3: Non-extensive diagram of variables in the quenching, solution preparation and ultrasonic spray coating steps, highlighting the variables selected for the two proposed studies.

4. Results and Discussion

4.1. Ultrasonic Spray Coating (OFAT)

For the OFAT study, a center point (CP) is selected based on a set of parameters which previously resulted in high quality perovskite films [18]. Then, the spray coating parameters are individually tested by using a lower and a higher value, while keeping all other parameters at the center point value. The considered parameters are flow rate (FR), hot plate temperature (HPT), path speed (PS), nitrogen pressure for the carrier gas (N2P), number of passes (#Passes), and nozzle-to-sample distance (NTSD). The position of the sample in the XY axis (along the hotplate) is kept constant as to align the center of the substrate with the linear movement performed by the mechanical arm. The center point is defined in **Table 1**. The solvent mixture used for the ink for these experiments is 80% DMF and 20% NMP, in volume. The quenching parameters are kept constant, with gas pressure of 7.6 bar (maximum) and distance of 5 cm between gun and substrate.

Table 1: Parameter values for the Center Point.

FR	HPT	PS	N2P	#Passes	NTSD
1 mL/min	40 °C	30 mm/sec	3 bar	1	10 cm

Number of Passes: To assess the effect of multiple passes, deposition experiments are performed by spraying up to 3 layers sequentially, with 30 seconds of drying time in between. The deposition of a second and third layers on previously deposited precursor film resulted in increasingly poor wetting, with the formation of irregular patches of material throughout the substrate. Optical microscopy combined with laser scanning revealed the accumulation of material in those spots, with the build-up of peaks and fiber-like radial structures (**Figure 4**). The formation of these defects is observed during deposition, before

the quenching step can be performed, and hence, would provide a clear disadvantage when carried on to the final perovskite film.

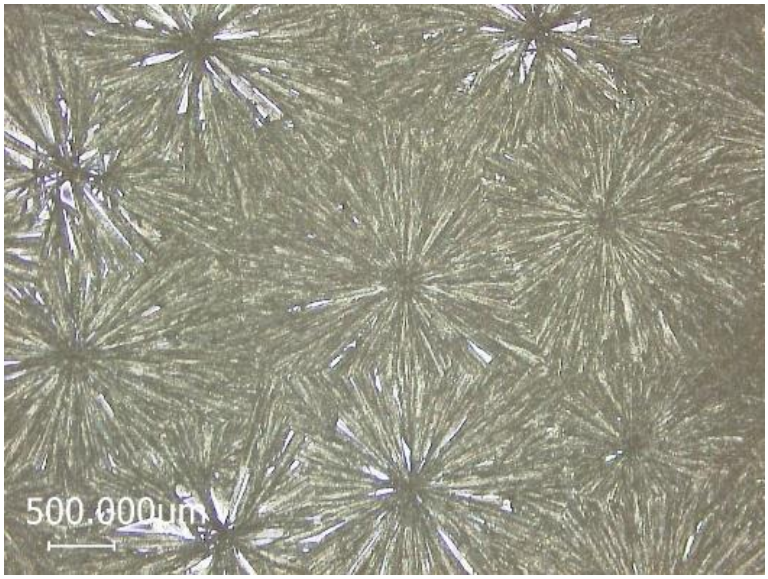

Figure 4: Optical microscopy image of a perovskite film after sequential deposition of 3 layers. Build-up of peaks in the center of fiber-like radial structures can be observed.

Nozzle-to-substrate distance: Next up, the positioning of the substrate in relation to the nozzle is studied in relation to the z-axis (orthogonal to the hot plate), with the x-y position of the substrate kept constant as to align its center to the spray path. This is done to avoid the need for patterning (movements of the nozzle in more than one direction), which could cause re-coating of the same area and the previously observed accumulation of material. The nozzle position in the z-axis ultimately result in a change of sprayed area: shorter distance results in a narrower covered area, and higher distance results in a wider covered area. It is noticeable that for higher distance, the quality of the spray is reduced, as the droplets must travel longer until reaching the substrate. This can be optimized by adjusting the carrier gas pressure, precursor flow rate and hot plate temperature. However, the 10 cm NTSD results in a path width slightly larger than 3 cm, ideal for coating the 3x3 cm substrate evenly with a single pass.

Nitrogen pressure: The flow of nitrogen gas on the auxiliary nozzle head is responsible for directing the droplets generated in the ultrasonic nozzle. The flow can be regulated by a built-in valve and measured in terms of pressure on the auxiliary line. This adjustment can be performed during deposition, and the effect of it on the spray is immediately visible: When the pressure is lower than a certain threshold - which corresponds to around 2 bar with other parameters at the CP – the resulting spray is irregular and fluctuates between horizontal and vertical flow. After the threshold the spray becomes stable and vertical flow is obtained. With increasing pressure, the ink droplets are accelerated faster into the substrate, which can cause outwards-flow patterns in resulting film. Such phenomenon is observed at pressures over 4 bar, with other parameters at the CP. Variations between 2 bar and 4 bar do not provoke visible changes in the spray nor in the produced film.

Hotplate temperature: As previously reported [18], spray coating at temperatures over 60 °C can cause the solvent to evaporate before forming a homogeneous wet layer, resulting in a non-uniform perovskite film. When spray coating with the hot plate turned off (25 °C), it was possible to see an excess of precursor solution around the substrate, which can infiltrate on the back surface of the glass slide and cause an accumulation of material on it (**Figure 5**). Although it does not damage the cell stack itself, this accumulated material is

difficult to remove completely, and causes light absorption losses, which is noticeable when measuring cell performance (**Tables 2 and 3**).

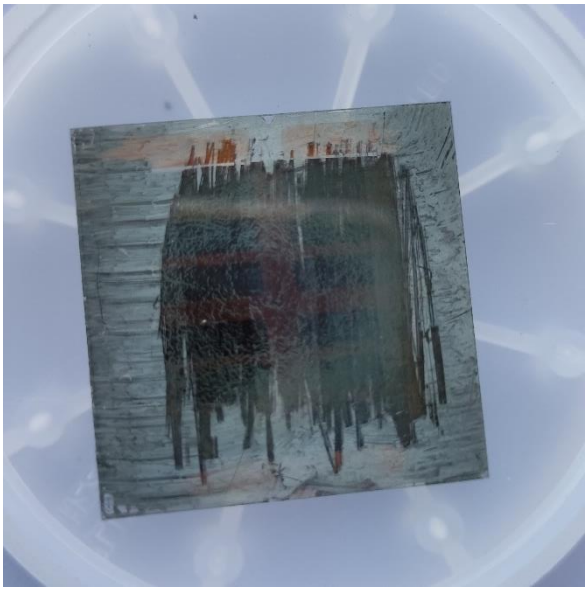

Figure 5: Sample with back-side infiltration, partially cleaned by scratching the perovskite away.

Path speed: Determining the speed at which the spraying nozzle passes through the substrate is one of the main ways of controlling the amount of solution deposited on it. For the path speed analysis three situations are studied: the center point (30 mm/sec), higher speed (45 mm/sec), and lower speed (15 mm/sec). **Table 2** summarises the results.

Table 2: Results summary of the Path Speed study.

Situation	Path Speed (mm/sec)	Uniform wet layer?	PCE (%)
CP+	45	Yes	13 ± 1
CP	30	Yes	14 ± 1
CP-	15	Soaked	8 ± 5

When the path speed is lower, more solution is sprayed in the same area. As in the case of low temperature deposition(**Figure 5**), the excess amount of solution infiltrates the back surface of the cell and causes perovskite to be deposited there. JV measurements showed a much lower power conversion efficiency in this case, as well as higher variance, which can be caused by the absorption losses on the back surface of the glass. The higher speed resulted in cells of a similar performance and visual properties to those of the center point, although with slightly lower power conversion efficiency.

Flow rate: The flow rate of ink during deposition is, like the path speed, a main factor on the amount of precursor solution deposited on the substrate. Additionally, it is also vital for maintaining a stable spray. A low flow rate (lower than 0.5 mL/min) can cause the spray to be irregular, with intermittent pumps of spray. For the flow rate analysis, the center point (1 mL/min) is compared to a minimum flow rate while maintaining a stable spray (0.5 mL/min) and a higher flow rate (1.5 mL/min). **Table 3** summarises the results.

Table 3: Results summary of the Flow Rate study.

Situation	Flow Rate (mL/min)	Uniform layer?	PCE (%)
CP+	1.5	Soaked	12 ± 1
CP	1	Yes	14 ± 1
CP-	0.5	No	-

The flow rate of 0.5 mL/min was not enough to fully cover the substrate with precursor solution, and therefore resulted in partial coverage and shunted solar cells. The higher flow rate caused substrate soaking and back surface accumulation of material, however in a lower degree than the low temperature and low path speed situations, which caused the produced cells to exhibit a power conversion efficiency only slightly lower than that of the center point cell.
The OFAT study revealed the importance of the spray coating parameters on the formation of a wet film of precursor solution. Moreover, many of the studied variables exhibited positive results (*i.e.*, a homogeneous wet layer is formed) over a range of values. The films produced within these ranges show limited variance in quality and performance, while processing outside of these ranges can result in the non-formation of a wet layer, resulting in heterogeneous films unsuitable for use as absorbing layers in solar cells.

4.2. Gas Quenching (Full Factorial)

Based on the results of the previous section, the center point parameters for the ultrasonic spray coating step are kept for the study of quenching parameters, as they corresponded to the highest efficiencies and lower variance in produced cell performances.
The experiments are designed to study the three key variables - distance between the air gun and the film (hereafter referred as “Distance”), gas (N_2) pressure, and solvent volatility, or volumetric percentage of NMP (NMP%). For each parameter, a low, middle, and high value are studied. Datapoints are referred as the abbreviation “x/y/z”, where “x” corresponds to the N_2 Pressure value, “y” to the Distance value, and “z” to the NMP% value (*e.g.* datapoint 7.6/5/10 refers to the set of samples quenched with 7.6 bar, gun distance of 5 cm, and with 10% NMP in the solvent mixture). In full factorial analyses, it is often the case that only the edges of and a central point are experimentally collected, with other data points calculated assuming a consistent trend in the in-between region. For this analysis, all 27 data points were experimentally collected. This is done because non-linear and hard-to-predict behaviour is of particular interest to fully understand how the parameters affect the produced film. With each datapoint consisting of an average between at least 15 individual solar cells, a statistical analysis software is used for better visualization of trends and patterns in the results. The responses in terms of solar cell performance and film morphology are presented and discussed in the respective following sections.

4.2.1. Performance

Four key performance indicators – efficiency, fill factor (FF), short circuit current (J_{sc}), and open circuit voltage (V_{oc}) – are determined via JV measurements of the produced cells. **Table 4** presents this data as the average of measured values for each datapoint.

Table 4: Average performance results per datapoint, determined after JV measurements, and ordered by decreasing efficiency.

Datapoint Abbreviation	Efficiency (%)	V_{oc} (mV)	FF (%)	J_{sc} (mA/cm^2)
7.6/2/15	14.8	949	69.7	22.3
7.6/2/10	13.9	990	65.7	21.4
7.6/2/20	13.5	945	68.9	20.7
5.7/2/10	13.4	963	66.2	21.9
7.6/5/10	13.1	960	64.3	21.2
5.7/2/15	13.0	943	65.9	20.9
3.8/2/10	12.9	924	64.4	21.6
5.7/5/10	12.4	900	61.2	22.4
5.7/2/20	11.9	879	63.6	21.0
3.8/2/15	11.4	945	62.3	19.4
7.6/8/10	11.2	915	59.3	20.7
3.8/2/20	10.3	838	60.3	19.6
7.6/5/15	9.6	812	57.3	20.0
7.6/5/20	9.5	814	57.4	20.2
5.7/5/15	8.4	858	54.7	17.8
5.7/5/20	6.9	709	50.3	18.5
5.7/8/20	6.4	673	48.4	19.1
5.7/8/15	6.2	732	48.9	17.8
3.8/5/20	5.5	615	44.8	18.1
3.8/8/15	5.5	653	45.1	18.6
3.8/5/15	5.0	610	44.9	18.2
5.7/8/10	4.6	489	39.3	21.7
3.8/8/20	4.2	624	40.1	16.8
7.6/8/15	4.2	530	39.8	18.5
3.8/5/10	3.9	479	37.0	19.7
7.6/8/20	3.8	516	40.5	17.9
3.8/8/10	1.5	285	31.3	18.0

By organizing the table from highest to lowest efficiencies, an initial evaluation of the datapoints can be made. Highest pressure and lowest distance produce the best performing cells, while the influence of the NMP amount is not as evident. Moreover, V_{oc} and fill factor follow a similar trend, while J_{sc} values are less linear in comparison to efficiency.
The measured values are then transferred to the statistical analysis software, and a prediction model is estimated for calculating solar cell efficiency based on the individual effects of the 3 studied variables, their quadratic value, as well as interactions between each two variables. A coefficient of determination (RSq) of 0.83 was obtained (**P-Values:** Distance = 0.000000009; Pressure = 0.00022; Pressure*NMP% = 0.04296; NMP% = 0.05954). Variables and interaction of variables with P-Value higher than 0.1 were removed from the model. All quadratic values were excluded from the model due to high P-values.

The P-Values of the kept variables confirm the higher impact of Pressure and Distance on the efficiency of the cells in the studied range, with Distance having the largest impact. The P-Values for NMP% and the interaction between pressure and NMP% are high, indicating a lower impact on cell efficiency. It is noteworthy, however, that the interaction between the two parameters has a slightly lower P-Value than the NMP% alone. This interaction can be further visualised by the prediction profiler function in the software, which allows a quick visualization of a parameter's response to a variation of the other parameter. As illustrated in **Figure 4**, this tool is used to show the difference in the curvature of the NMP% x Efficiency graph when the Pressure is changed from low to high. This reveals that NMP% has a significant impact on efficiency when processing with high gas pressure (lower amount of NMP resulted in higher efficiencies), but this impact is reduced when processing with low gas pressure, as the efficiency is almost constant for all values of NMP%.

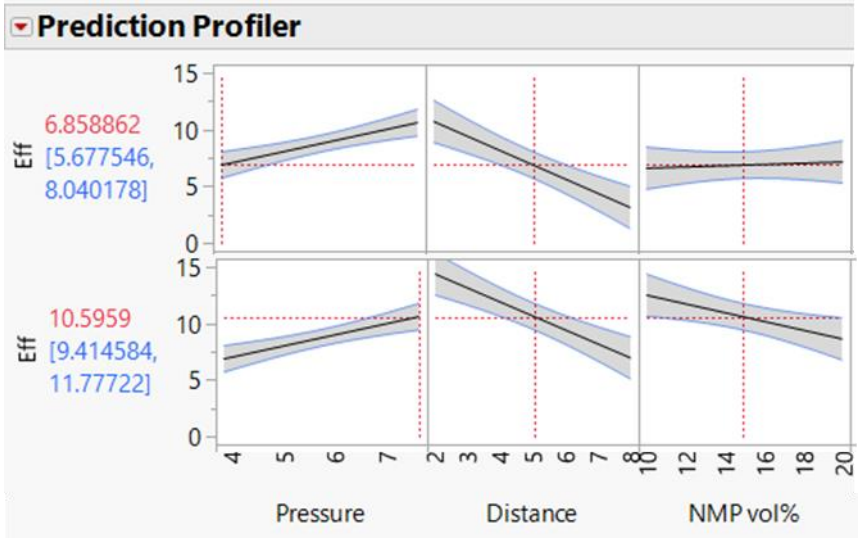

Figure 6: Prediction Profiler for the efficiency prediction model in two situations: top corresponds to the low-pressure situation; bottom corresponds to the high-pressure situation. A change in curvature for the Efficiency vs NMP% plot is observed.

A similar approach is used to understand the impact of the variables and their interactions on the fill factor, V_{oc} and J_{sc}. The fill factor model is especially close to the efficiency model, with an RSq of 0.81 (**P-Values:** Distance = 0.00000002; Pressure = 0.00053; Pressure*NMP% = 0.07512; NMP% = 0.53571). The P-values follow and same order of importance for the variables as the efficiency model, with Distance being the most impactful, followed by Pressure, NMP%*Pressure, and NMP%. The V_{oc} model diverged in the magnitude of the P-value for most variables, which resulted in a less precise prediction, with RSq of 0.73 (**P-Values:** Distance = 0.000003; Pressure = 0.00506; Pressure*NMP% = 0.01774; Distance*NMP% = 0.38134; NMP% = 0.53584). With the high P-value of NMP% for the fill factor and V_{oc} models, it becomes more challenging to draw conclusions about this variable and its interactions based on the models alone. However, the Pressure*NMP% interaction could be observed having a similar nature as in the efficiency model.
Lastly, the prediction model for J_{sc} is the most divergent one. It has RSq of 0.68, the lowest of all models (**P-Values:** Distance = 0.000001; NMP% = 0.00411; Pressure = 0.01534). The order of the P-value of the variables is changed in comparison to the efficiency model, with NMP% being now more impactful than Pressure. Moreover, the interaction between Pressure and NMP% is not observed, as all interactions have high P-values (>0.1) and, therefore, are excluded from the model.
Based on these results, we see a strong relation between efficiency, V_{oc} and fill factor, with the low Distance and high Pressure being the most influential factors on generating films that result in cells with high performance. To further investigate how the different processing conditions affect the device performance, a smaller set of datapoints is selected for further

characterization studies. Since the NMP% had the least influence in the observed performance, the value of 15% is kept constant, and the 9 correspondent datapoints (x/y/15) are studied. External quantum efficiency measurements (**Figure 7**) are used to verify how the devices interact with the incident photons, allowing for a more precise estimation of the short circuit current and the determination of bandgap energy (E_g), as proposed by L. Krückemeier *et. al.* [34]. Additionally, JV measurements in forward and reverse scan (**Figure 8**) allow the assessment of the hysteresis level on the studied devices. A representative cell with efficiency closest to the datapoint's average is selected in each device for the EQE and JV measurements.

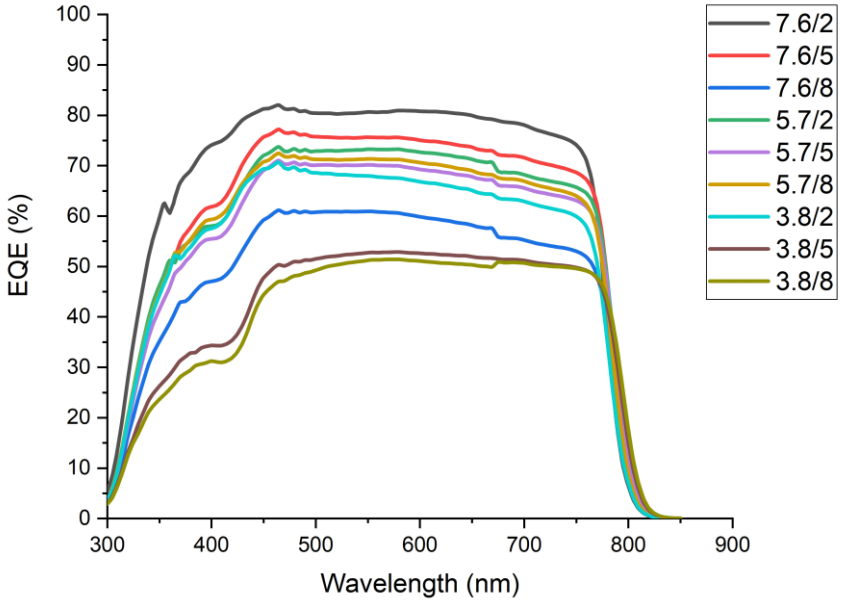

Figure 7: External quantum efficiency measurements of the 9 cells representing the datapoints "x/y/15".

Two steps can be seen in the EQE curve in most of the studied cells. The smaller step at the wavelength of 670 nm is due to a change in lamp on the measuring setup. The larger step, which occurs between 400 and 450 nm, is more intense in datapoints with lower performance, and could be associated with a presence of structural defects in the interface between the perovskite and the NiOx layer. This is further discussed in the next section, with the analysis of the cross-section SEM images of the films. Moreover, the EQE is overall lower in datapoints corresponding to lower N_2 pressure and higher air gun distance. This is expected as these parameters were found to generate lower performing cells. The analysis of the EQE data also allows the determination of the J_{sc}, as well as the bandgap of the solar cells. The results of these calculations, as well as the updated PCE, are presented in **Table 5**.

Table 5: Comparison of performance determined by EQE and JV measurement (**Figure 6**) of the 9 cells representing the datapoints "x/y/15".

Sample	**Solar Simulator**				**EQE**		
	V_{oc} (V)	**FF (%)**	**J_{sc} (mA/cm^2)**	**PCE (%)**	**J_{sc} (mA/cm^2)**	**PCE (%)**	**Bandgap**
7.6/2	1.04	64.83	21.5	14.5	20.3	13.7	1.59

7.6/5	0.95	53.76	18.4	9.4	18.9	9.7	1.58
7.6/8	0.87	51.11	15.9	7.1	14.9	6.6	1.57
5.7/2	0.89	59.87	20.0	10.7	18.2	9.7	1.57
5.7/5	0.93	54.87	17.5	8.9	17.5	8.9	1.57
5.7/8	0.78	48.62	17.9	6.8	17.7	6.7	1.58
3.8/2	0.93	53.72	17.2	8.6	16.8	8.4	1.58
3.8/5	0.85	43.56	14.5	5.4	13.2	4.9	1.56
3.8/8	0.69	39.6	12.8	3.5	12.8	3.5	1.55

Most of the J_{sc} determined by EQE differ from those determined by JV measurement by less than 1.5 mA/cm^2. This shows that the solar simulator measurements can result in a slight overestimation of both J_{sc} and PCE. Nevertheless, the comparison between the performance of each datapoint results in the same conclusions, since the order of highest to lowest performance is not altered (*i.e.,* high pressure and low distance continue to provide the best working cells). Moreover, the bandgap determination reveals similar bandgap energies for the 9 datapoints, with a slight decrease in the lower performing cells.

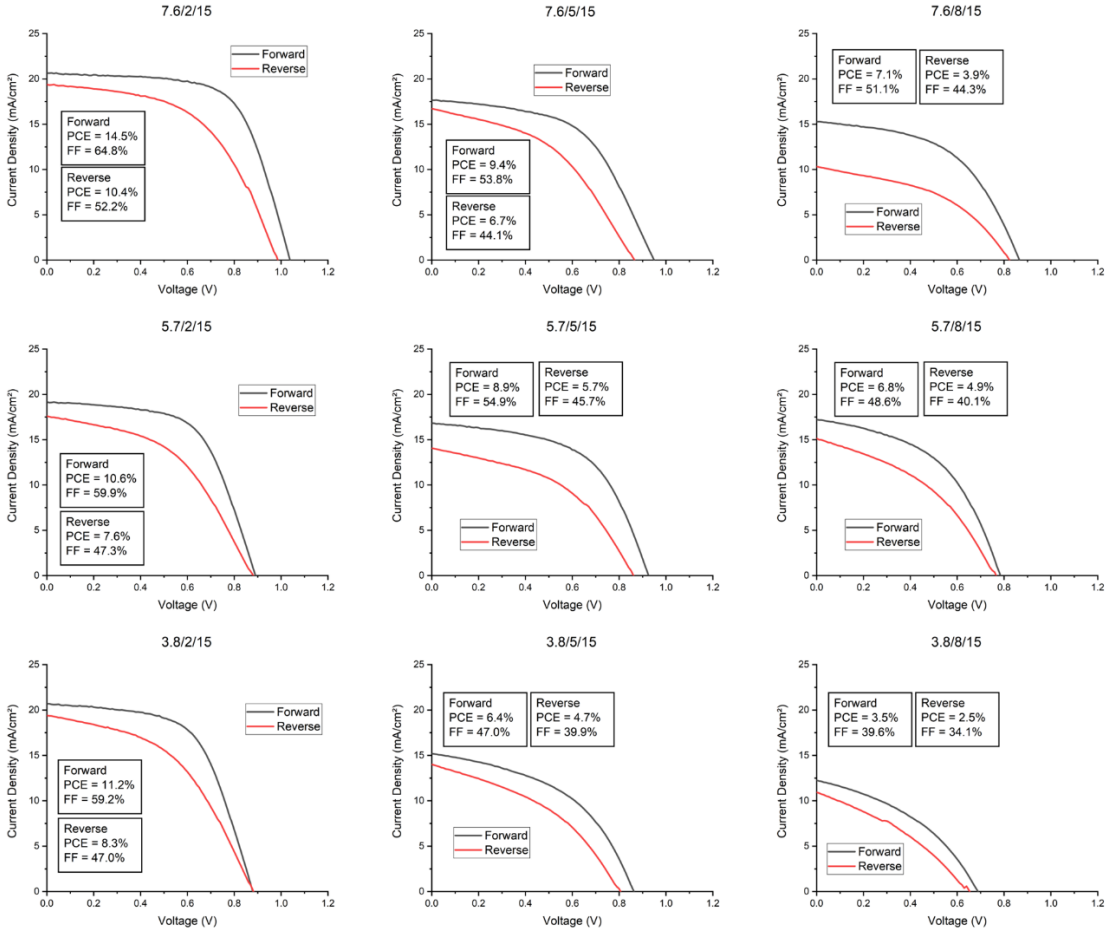

Figure 8: JV curves of the 9 cells representing the datapoints “x/y/15”.

The reverse scan of the selected cells reveals a high degree of hysteresis in all devices. The hysteresis index (HI) can be calculated as described below, with PCE_f being the PCE of the cell in forward scan, and PCE_r the PCE in reverse scan. The HI is similar for most of the cells (between 0.26 and 0.29), with cell 5.7/5 and 7.6/8 having higher HI: 0.35 and 0.45, respectively. It is noteworthy that the observed hysteresis can depend on the speed of measurement [35], and the curves presented herein might not correspond to the steady

state conditions of the cells. With that, further investigation is needed to assess the exact level of hysteresis and determine the causes and possible solutions for it.

$$HI = \frac{PCE_f - PCE_r}{PCE_f}$$

4.2.2. Thickness

A representative sample of each datapoint is produced up to the annealing of the perovskite layer and inspected via scanning electron microscopy. Cross section pictures of the center of the samples permitted the estimation of the perovskite layer thickness. The region considered is the one containing the ITO stripes, where solar cells would be produced in the case of finalized devices. **Figure 9** illustrates this process for three datapoints. The estimated thickness for all datapoints is presented in **Table 6**, in order of decreasing thickness.

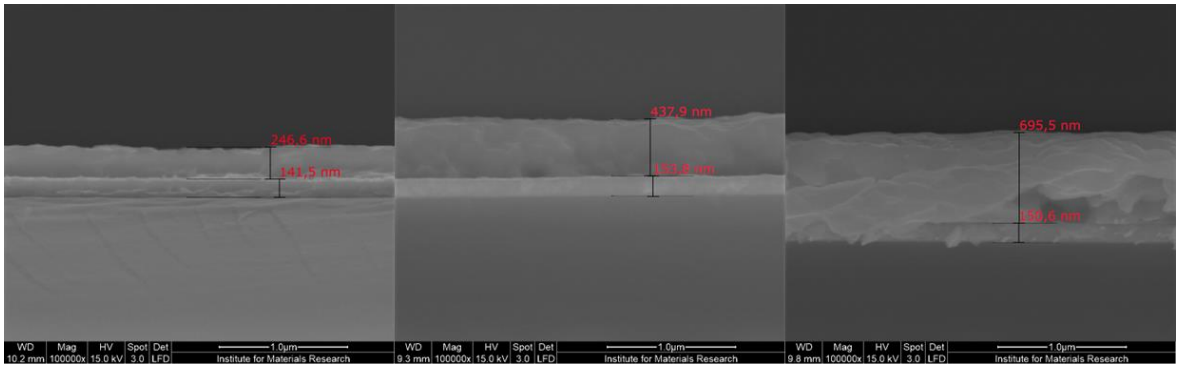

Figure 9: Thickness determination by cross sectional SEM. From left to right, the images correspond to the following datapoints: 3.8/2/15; 5.7/5/15; 7.6/8/15.

Table 6: Determined thickness per datapoint, ordered by decreasing thickness.

Datapoint Abbreviation	FF (%)	J_{sc} (mA/cm2)	V_{oc} (mV)	Efficiency (%)	Thickness (nm)
7.6/8/10	59.3	20.7	915	11.2	967
5.7/8/20	48.4	19.1	673	6.4	870
3.8/8/15	45.1	18.6	653	5.5	741
3.8/8/20	40.1	16.8	624	4.2	727
7.6/8/15	39.8	18.5	530	4.2	695
7.6/8/20	40.5	17.9	516	3.8	677
5.7/8/10	39.3	21.7	489	4.6	671
7.6/5/10	64.3	21.2	960	13.1	609
3.8/5/15	44.9	18.2	610	5.0	585
3.8/2/20	60.3	19.6	838	10.3	576
5.7/5/10	61.2	22.4	900	12.5	560
7.6/5/15	57.3	20.0	812	9.6	551
5.7/8/15	48.9	17.8	732	6.2	550
3.8/8/10	31.3	18.0	285	1.5	533
3.8/5/10	37.0	19.7	479	3.9	511

3.8/5/20	44.8	18.1	615	5.5	509
5.7/5/20	50.3	18.5	709	6.9	485
7.6/5/20	57.4	20.2	814	9.5	475
5.7/2/20	63.6	21.0	879	11.9	445
5.7/5/15	54.7	17.8	858	8.4	437
7.6/2/10	65.7	21.4	990	13.9	408
3.8/2/10	64.4	21.6	924	12.9	379
5.7/2/10	66.2	21.9	963	13.4	338
7.6/2/15	69.7	22.3	949	14.8	333
7.6/2/20	68.9	20.7	945	13.5	302
5.7/2/15	65.9	20.9	943	13.0	266
3.8/2/15	62.3	19.4	945	11.4	246

The results of this study initially show a strong correlation between the Distance parameter and film thickness. Up next, a prediction model for thickness is generated, again using the 3 variables, their quadratic values, and their interactions. The resulting model has RSq of 0.79 (**P-Values:** Distance = 0.0000001; Pressure*NMP% = 0.00872; Pressure*Distance = 0.13089; Pressure = 0.59277; Distance*NMP% = 0.76481; NMP% = 0.819590). Quadratic values are again excluded from the model due to high P-values. The model confirms the important role of air gun distance in the final film thickness, with the other two individual parameters exhibiting high P-values. The interaction effect between Pressure and NMP% reveals that in low pressure, thickness increases with NMP%, while in high pressure it decreases. Likewise, for low NMP%, thickness increases with pressure, while for high NMP% the thickness decreases with increasing pressure.
Comparing film thickness with the previously determined solar cell performance, a soft trend can be seen. Thickness between 250 and 410 nm corresponded to datapoints with consistently higher cell efficiency, while the lowest efficiencies are observed in datapoints with higher thickness (650 to 900 nm). Similar trends are observed for J_{sc}, V_{oc} and fill factor. These trends do not follow previous observations in literature, which revealed an increase in efficiency when perovskite thickness was brought closer to 600 nm by changing only the solution concentration [18, 23]. Moreover, the datapoints that have efficiencies higher than 10% despite having thickness above 600 nm were produced with high N_2 pressure (such as datapoints 7.6/8/10 and 7.6/5/10). These findings suggest the presence of additional factors for determining the quality of the produced films. Comparing the three films in **Figure 10** it is notable that the thicker films have a few dark spots in the NiOx/Perovskite interface. This might suggest the presence of structural defects, which aligns with the 400-450 nm step observed in the EQE curves of such films (**Figure 7**).The quality of the films and the presence of defects are further discussed in the next section, after the top view analysis of the films.

4.2.3. Grain Size

Top view SEM images of the produced perovskite layer are inspected to determine average grain size. Larger grains are typically associated with higher quality films and better photovoltaic efficiency. This is due to the lesser amount of grain boundaries, as those can cause electronic trap states and undesired charge-carrier recombination [36]. The grain size determination is performed following a developed framework comprised of a sequence of image processing treatments and use of Fiji software [37]. **Figure 10** illustrates a representative outcome for the grain outlines in datapoint 7.6/2/10. Grains which are only partially inside the borders of analysis are overlooked. The result for grain sizes of all datapoints, in terms of average diameter, is given in **Table 7**.

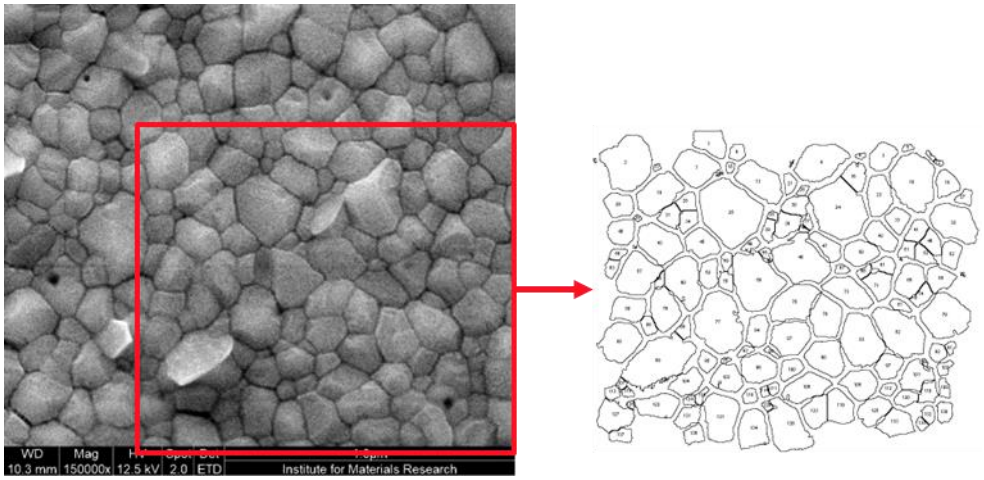

Figure 10: Representation of image treatment for grain size determination.

Table 7: Determined grain size per datapoint, in terms of average diameter, ordered by decreasing grain size.

Datapoint Abbreviation	FF (%)	J_{sc} (mA/cm2)	V_{oc} (mV)	Efficiency (%)	Avg. Grain Diameter (nm)
3.8/8/15	45.1	18.6	653	5.5	164
5.7/8/15	48.9	17.8	732	6.2	154
3.8/5/15	44.9	18.2	610	5.0	151
7.6/8/15	39.8	18.5	530	4.2	145
3.8/8/20	40.1	16.8	624	4.2	135
5.7/5/15	54.7	17.8	858	8.4	134
3.8/2/20	60.3	19.6	838	10.3	129
3.8/2/15	62.3	19.4	945	11.4	125
7.6/5/15	57.3	20.0	812	9.6	123
7.6/8/20	40.5	17.9	516	3.8	121
5.7/2/20	63.6	21.0	879	11.9	116
5.7/5/20	50.3	18.5	709	6.9	115
5.7/8/20	48.4	19.1	673	6.4	113
5.7/2/15	65.9	20.9	943	13.0	109
3.8/5/20	44.8	18.1	615	5.5	106
7.6/2/15	69.7	22.3	949	14.8	98
7.6/5/20	57.4	20.2	814	9.5	98
3.8/8/10	31.3	18.0	285	1.5	95
3.8/5/10	37.0	19.7	479	3.9	88
3.8/2/10	64.4	21.6	924	12.9	83
5.7/8/10	39.3	21.7	489	4.6	77
7.6/2/20	68.9	20.7	945	13.5	76

7.6/5/10	64.3	21.2	960	13.1	75
5.7/2/10	66.2	21.9	963	13.4	66
5.7/5/10	61.2	22.4	900	12.5	65
7.6/2/10	65.7	21.4	990	13.9	65
7.6/8/10	59.3	20.7	915	11.2	64

Based on these results, one initial observation is the influence of NMP% on grain size. Larger grains were produced with 15% NMP in volume, while 10% produced overall smaller grains. The higher concentration of 20% generated intermediary sizes, indicating a non-linear relation. The prediction model resulted in high RSq of 0.89 (**P-Values:** NMP%*NMP% = 0.000000007; NMP% = 0.0000003; Pressure = 0.00014; Distance = 0.00026). The quadratic interaction NMP%*NMP% had the lowest P-value, being the first instance in which a quadratic value of one of the variables was kept in the model. On top of the high influence of NMP% on the grain size, Pressure and Distance show a dimmer linear influence, with lower pressure and higher distance correlating to larger grain size.
Analogously to the thickness analysis, the comparison of grain size and cell performance shows unexpected results, with a trend of larger grain size corresponding to lower efficiency, V_{oc}, J_{sc}, and fill factor in the majority of the datapoints. Typically, higher grain sizes and lower density of grain boundaries correspond to less trap states, which can cause undesired charge recombination and reduced performance. To better understand why this was not observed here, a qualitative analysis of the SEM pictures is performed, with special focus on structural defects. **Figure 11** exemplifies the defects observed in this process, and **Table 8** identifies in which images such defects were observed.

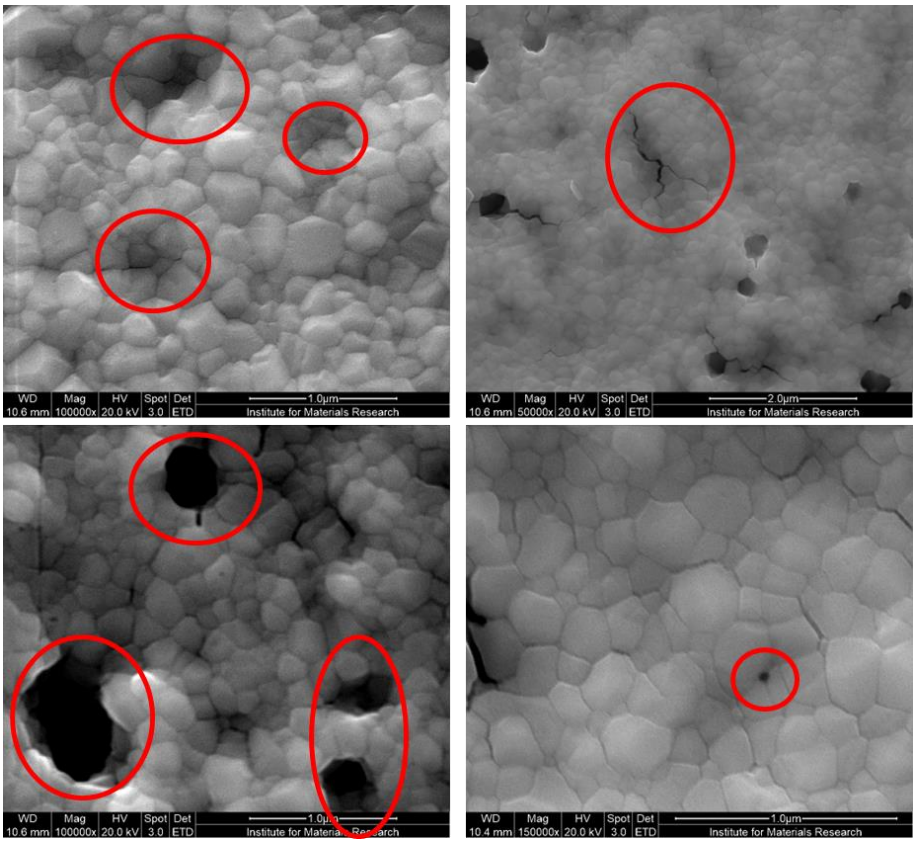

Figure 11: Examples of detected structural defects. Top-left: shaded spots; Top-right: crack; Bottom-left: Pores; Bottom-right: pin hole.

Table 8: Observed defects per datapoint, ordered by increasing efficiency.

Datapoint Abbreviation	FF (%)	J_{sc} (mA/cm2)	V_{oc} (mV)	Efficiency (%)	Avg. Grain Diameter (nm)	Observed defects (in a 4 μm^2 area)
3.8/8/10	31.3	18.0	285	1.5	95	3 large pores 1 dark spot >10 cracks 1 pin hole
7.6/8/20	40.5	17.9	516	3.8	121	1 large pore 2 cracks 2 shaded spots
3.8/5/10	37.0	19.7	479	3.9	88	1 crack 1 shaded spot
7.6/8/15	39.8	18.5	530	4.2	145	1 crack 1 shaded spot
3.8/8/20	40.1	16.8	624	4.2	135	1 pore 2 cracks
5.7/8/10	39.3	21.7	489	4.6	77	3 pores 3 cracks
3.8/5/15	44.9	18.2	610	5.0	151	2 pores 3 shaded spots
3.8/8/15	45.1	18.6	653	5.5	164	1 pore 7 cracks 2 shaded spots 2 pin holes
3.8/5/20	44.8	18.1	615	5.5	106	5 shaded spots
5.7/8/15	48.9	17.8	732	6.2	154	2 pores 3 shaded spots
5.7/8/20	48.4	19.1	673	6.4	113	1 large pore 2 shaded spots
5.7/5/20	50.3	18.5	709	6.9	115	4 pores 5 cracks 2 shaded spots
5.7/5/15	54.7	17.8	858	8.4	134	4 shaded spots
7.6/5/20	57.4	20.2	814	9.5	98	1 crack 2 pin holes
7.6/5/15	57.3	20.0	812	9.6	123	3 shaded spots
3.8/2/20	60.3	19.6	838	10.3	129	2 cracks 1 shaded spot 1 pin hole
7.6/8/10	59.3	20.7	915	11.2	64	1 pin hole
3.8/2/15	62.3	19.4	945	11.4	125	2 pin holes
5.7/2/20	63.6	21.0	879	11.9	116	2 cracks 2 pin holes
5.7/5/10	61.2	22.4	900	12.5	65	1 shaded spot
3.8/2/10	64.4	21.6	924	12.9	83	3 pin holes 2 small cracks
5.7/2/15	65.9	20.9	943	13.0	109	-
7.6/5/10	64.3	21.2	960	13.1	75	2 pin holes

5.7/2/10	66.2	21.9	963	13.4	66	-
7.6/2/20	68.9	20.7	945	13.5	76	1 pin hole
7.6/2/10	65.7	21.4	990	13.9	65	5 pin holes
7.6/2/15	69.7	22.3	949	14.8	98	-

Although the analysed area is only a partial representation of each sample, the much higher number of defects in datapoints with poorly performing cells indicates they might be the cause for this low performance. On top of that, the high porosity can cause an expansion of the film thickness, which can lead to the higher observed layer thickness in datapoints with more observed defects and low efficiency cells. The presence of structural defects often causes higher probability of charge carrier recombination, which generate a decrease in V_{oc} [36]. The same is not observed in the more compact layers with higher V_{oc} (**Table 7**). Regarding the impact of the defects on grain size, one possible explanation is that due to the presence of empty spots, the grains have more space to grow during the annealing step, however additional investigation is needed to comprehend the relation between defect density and grain size, such as in situ monitoring of grain growth.
Furthermore, to better understand how the thickness and the presence of defects affect the light absorption on these films, the 9 datapoints previously selected for EQE measurements (x/y/15) are also studied by reflection (R) and transmission (T) measurements (**Figures 12 and 13**). This enables the construction of the absorption (A) spectra (**Figure 14**) of the 9 devices (A = 100 – R – T).

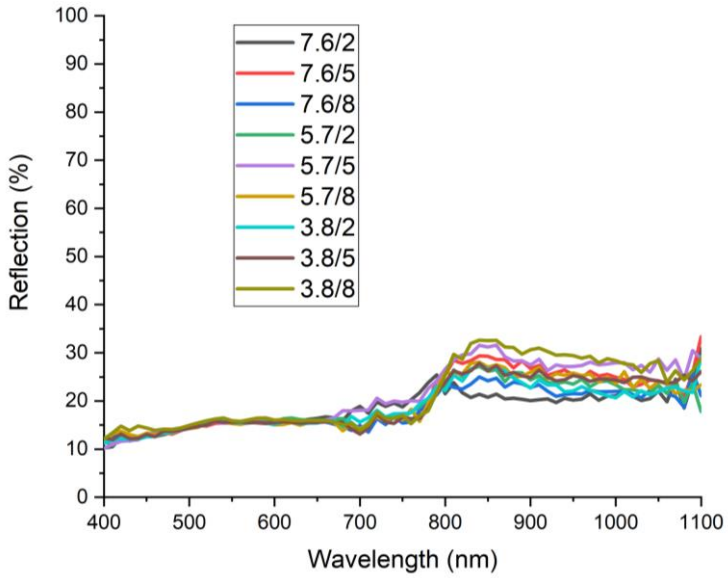

Figure 12: Reflection measurements of the 9 samples representing the datapoints “x/y/15”.

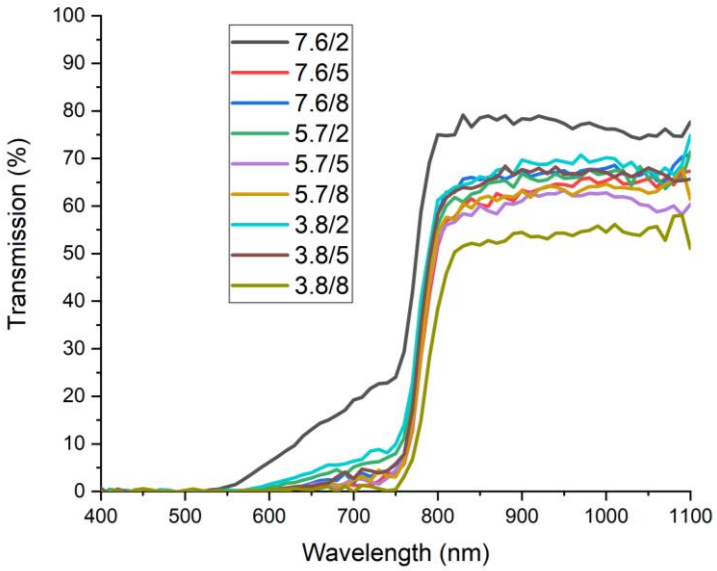

Figure 13: Transmission measurements of the 9 samples representing the datapoints “x/y/15”.

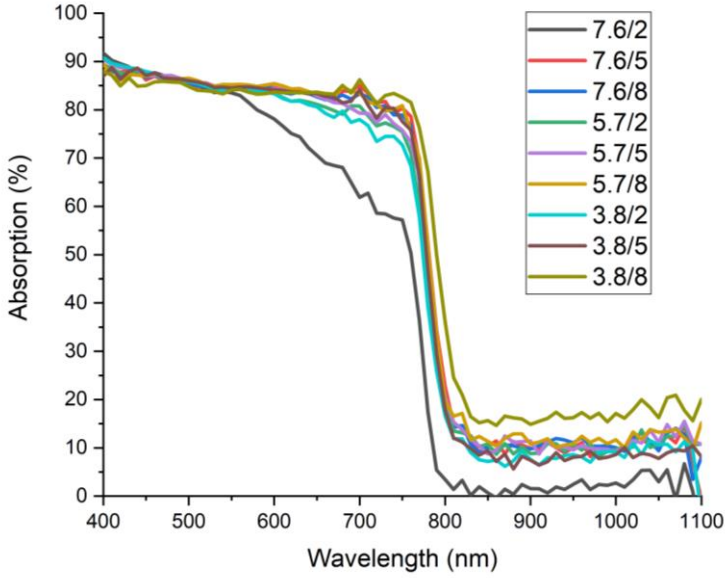

Figure 14: Calculated absorption (100 - reflection - transmission) of the 9 samples representing the datapoints “x/y/15”.

The reflection measurements (**Figure 12**) reveal a similar behaviour for the 9 samples, especially in the region before 800 nm wavelength, which is the most relevant for the operation of the perovskite solar cells. The transmission spectra (**Figure 13**), on the other hand, show that the best cell (7.6/2) has a significantly distinct optical behaviour. In this cell, the gradual increase in transmission between 550 and 750 nm indicates the film is failing to absorb all available light. This can be a consequence of the film being too thin, with expected thickness around 330 nm (**Table 6**), instead of the desired 600 nm. Hence, the performance of these devices can be increases considerably, if the thickness is raised to 600 nm, while

maintaining the film quality. Moreover, the higher absorption of lower performing cells (*e.g.*, sample 3.8/8 in **Figure 14**) indicates that a significantly larger portion of the absorbed photons is being lost in these devices, without generating current. This is possibly due to the large density of structural defects in these perovskite films.

5. Conclusions

The systematic study of the ultrasonic spray coating of perovskite layers using a design of experiment approach allowed for a deeper understanding of the process variables and their implication on the quality of fabricated films and solar cells. The one factor at a time investigation of the ultrasonic spray coating parameters revealed their importance on the formation of a uniform wet layer of precursor solution. The full factorial analysis on the gas quenching step permitted the assessment of the impact of air gun distance from the substrate, solvent volatility, and gas pressure on the morphology of crystallized perovskite films and their performance as the active layer of solar cells. This study offers pathways for optimization of perovskite device fabrication. The distance between sample and air gun was shown to be the most impactful parameter for producing high-quality films and better performing devices, with gas pressure also playing an important role.
The best results were obtained by using the distance of 2 cm between the air gun and the sample, the highest N_2 pressure available on the setup (7.6 bar), and the solvent mixture with 15% NMP in volume. This combination of parameters resulted in the fabrication of compact crystalline perovskite layers, which exhibited the best performance as absorbing layers in solar cells, reaching an average efficiency of 14.8%.
Moreover, the morphology analysis led to the conclusion that the three parameters studied should be optimized to generate compact layers, instead of focusing on the apparent thickness, since higher thickness was caused by increased porosity and irregularities in the film. To reach the optimal thickness of 600 nm and improve the absorption of the perovskite layers, other parameters must be studied, such as the precursor solution concentration. An alternative route is layer stacking, with the deposition of other perovskite layers on top of the first crystallized layer, however additional steps must be taken to prevent the negative effects of recrystallization. Additionally, the high performing thin layers obtained in this study (thicknesses between 200 and 300 nm) could be considered for the application in semi-transparent photovoltaic devices [38], after further optimization.
With this successful proof of concept, design of experiments should be highly considered for the optimization and upscaling up of perovskite film fabrication. The high time-consumption of full factorial studies can be mitigated by a combination of process automation and emerging concepts for data analysis and optimization, such as machine learning.

Acknowledgements

This study was supported by the Special Research Fund (BOF) of Hasselt University, BOF number: BOF19OWB17. This project has also received funding from the European Union's Horizon 2020 research and innovation program under grant agreement Nº. 850937. S.H. acknowledges financial support by the Flanders Research Foundation (FWO)—strategic basic research doctoral grant 1S31922N. P.V acknowledges financial support by the Flanders Research Foundation Flanders (FWO)—strategic basic research doctoral grant 1S99121N.

References

[1] Tollefson, J. What the war in Ukraine means for energy, climate and food. *Nature* **2022**, 604, 232-233. https://doi.org/10.1038/d41586-022-00969-9

[2] Umar, M., Riaz, Y., Yousaf, I., Impact of Russian-Ukraine war on clean energy, conventional energy, and metal markets: Evidence from event study approach. *Resources Policy* **2022**, 79, 102966. https://doi.org/10.1016/j.resourpol.2022.102966
[3] NREL Efficiency Chart. https://www.nrel.gov/pv/cell-efficiency.html (Accessed on Dec, 2022).
[4] Moore, T. D.; Sai, H.; Tan, K. W.; Smilgies, D-M.; Zhang, W.; Snaith, H. J.; Wiesner, U.; Estroff, L. A. Crystallization Kinetics of Organic–Inorganic Trihalide Perovskites and the Role of the Lead Anion in Crystal Growth *J. Am. Chem. Soc.* **2015**, 137 (6), 2350–2358. https://doi.org/10.1021/ja512117e
[5] Walsh, A., Principles of Chemical Bonding and Band Gap Engineering in Hybrid Organic–Inorganic Halide Perovskites. *J. Phys. Chem. C* **2015**, 119 (11), 5755–5760. https://doi.org/10.1021/jp512420b
[6] Min, H., Lee, D.Y., Kim, J.; Kim, G.; Lee, K. S.; Kim, J.; Paik, M. J.; Kim, Y. K.; Kim, K. S.; Kim, M. G.; Sjin, T. J.; Seok, S. I. Perovskite solar cells with atomically coherent interlayers on SnO_2 electrodes. *Nature* **2021**, 598, 444–450. https://doi.org/10.1038/s41586-021-03964-8
[7] Duan, L.; Uddin, A. Defects and stability of perovskite solar cells: a critical analysis. *Mater. Chem. Front.* **2022**, 6, 400-417. https://doi.org/10.1039/D1QM01250A
[8] Das, S.; Yang, B.; Gu, G.; Joshi, P. C.; Ivanov I. N.; Rouleau, C. M.; Aytug, T.; Geohegan, D. B.; Xiao, K. High-Performance Flexible Perovskite Solar Cells by Using a Combination of Ultrasonic Spray-Coating and Low Thermal Budget Photonic Curing. *ACS Photonics* **2015**, 2 (6), 680-686. https://doi.org/10.1021/acsphotonics.5b00119
[9] Tait, J. G.; Manghooli, S.; Qiu, W.; Rakocevic, L.; Kootstra, L.; Jaysankar, M.; Masse de la Huerta, C. A.; Paetzold, U.W.; Gehlhaar, R.; Cheyns, D.; Heremans, P.; Poortmans J. Rapid composition screening for perovskite photovoltaics via concurrently pumped ultrasonic spray coating. *J. Mater. Chem. A.* **2016**, 4, 3792-3797 https://doi.org/10.1039/C6TA00739B
[10] Mohamad, D. K.; Griffin, J.; Bracher, C.; Barrows, A. T.; Lidzey, D. G. Spray-Cast Multilayer Organometal Perovskite Solar Cells Fabricated in Air. *Adv. Energy Mater.* **2016**, 6, 1600994. https://doi.org/10.1002/aenm.201600994
[11] Cassella, E. J.; Spooner, E. L. K.; Thornber, T.; O'Kane, M. E.; Catley, T. E.; Bishop, J. E.; Smith, J. A.; Game, O. S.; Lidzey, D. G. Gas-Assisted Spray Coating of Perovskite Solar Cells Incorporating Sprayed Self-Assembled Monolayers. *Adv. Sci.* **2022**, 9, 2104848. https://doi.org/10.1002/advs.202104848
[12] Yang, F.; Jang, D.; Dong, L.; Qiu, S.; Distler, A.; Li, N.; Brabec, C. J.; Egelhaaf, H.-J. Upscaling Solution-Processed Perovskite Photovoltaics. *Adv. Energy Mater.* **2021**, 11, 2101973. https://doi.org/10.1002/aenm.202101973
[13] Yang, Z.; Liu, Z.; Ahmadi, V.; Chen, W.; Qi, Y. Recent Progress on Metal Halide Perovskite Solar Minimodules. *Sol. RRL.* **2022**, 6, 2100458 https://doi.org/10.1002/solr.202100458
[14] Hamtaei, S.; Brammertz, G.; Kohl, T.; Buldu, D. G.; Birant, G.; de Wild, J.; Meuris, M.; Poortmans, J.; Vermang, B.. Investigating the experimental space for two-step Cu(In,Ga)(S,Se)2 absorber layer fabrication: A design of experiment approach. *Thin Solid Films* **2021**, 738, 138958. https://doi.org/10.1016/j.tsf.2021.138958
[15] Cao, B.; Adutwum, L. A.; Oliynyk, A. O.; Luber, E. J.; Olsen, B. C.; Mar, A.; Buriak, J. M. How To Optimize Materials and Devices via Design of Experiments and Machine Learning: Demonstration Using Organic Photovoltaics. *ACS Nano* **2018**, 12 (8), 7434-7444. https://doi.org/10.1021/acsnano.8b04726
[16] Baker, R. W.; Forfar, L.; Liang, X.; Cameron, P. J. Using design of experiment to obtain a systematic understanding of the effect of synthesis parameters on the properties of perovskite nanocrystals. *React. Chem. Eng.* **2021**, 6, 709-719. https://doi.org/10.1039/D0RE00149J
[17] Liu, H.; Chen, Q.; Wu, F.; Liu, X. Pyrene Core-based Dopant-free Hole Transporting Materials for Perovskite Solar Cells: A Theoretical Design and Experimental Verification. *J. Phys. Chem. C* **2022**, 126 (1), 160-168. https://doi.org/10.1021/acs.jpcc.1c09845

[18] Silvano, J.; Sala, J.; Merckx, T.; Kuang, Y.; Verding, P.; D'Haen, J.; Aernouts, T.; Vermang, B.; Deferme, W. A study of quenching approaches to optimize ultrasonic spray coated perovskite layers scalable for PV. *EPJ Photovolt.* **2022**, 13, 12. https://doi.org/10.1051/epjpv/2022008
[19] Kim, H.; Kim, H.; Park, N. Progress of Perovskite Solar Modules. *Adv. Energy Sustainability Res.* **2021**, 2, 2000051. https://doi.org/10.1002/aesr.202000051
[20] Jiang, Z.; Wang, B.; Zhang, W.; Yang, Z.; Li, M.; Ren, F.; Imran, T.; Sun, Z.; Zhang, S.; Zhang, Y.; Zhao, Z.; Liu, Z.; Chen, W. Solvent engineering towards scalable fabrication of high-quality perovskite films for efficient solar modules. *J. of Energy Chem.* **2023**, 80, 689-710. https://doi.org/10.1016/j.jechem.2023.02.017
[21] Cassella, E. J.; Spooner, E. L.; Smith, J. A.; Thornber, T.; O'Kane, M. E.; Oliver, R. D.; Catley, T. E.; Choudhary, S.; Wood, C. J.; Hammond, D. B.; Snaith, H. J.; Lidzey, D. G. Binary Solvent System Used to Fabricate Fully Annealing-Free Perovskite Solar Cells. *Adv. Energy Mater.* **2023**, 13, 2203468. https://doi.org/10.1002/aenm.202203468
[22] T. Feurer, A.N. Tiwari, Adv. Energy Mater. **9**, 1901428 (2019) https://doi.org/10.3929/ethz-b-000389221
[23] Song, W.; Zhang, X.; Lammar, S.; Qiu, W.; Kuang, Y.; Ruttens, B.; D'Haen, J.; Vaesen, I.; Conard, T.; Abdulraheem, Y.; Aernouts, T.; Zhan, Y.; Poortmans, J. Critical Role of Perovskite Film Stoichiometry in Determining Solar Cell Operational Stability: A Study on the Effects of Volatile A-Cation Additives. *ACS Appl. Mater. Interfaces* **2022**, 14 (24), 27922–27931. https://doi.org/10.1021/acsami.2c05241
[24] Park, J-W.; Park, J-W.; Jung, K.; Yang, M. K.; Lee, J-K. Influence of oxygen content on electrical properties of NiO films grown by rf reactive sputtering for resistive random-access memory applications. *Journal of Vacuum Science & Technology B: Microelectronics and Nanometer Structures Processing, Measurement, and Phenomena* **2006**, 24, 2205-2208. https://doi.org/10.1116/1.2244540
[25] Pintor-Monroy, M. I.; Murillo-Borjas, B. L.; Catalano, M.; Quevedo-Lopez, M. A. Controlling Carrier Type and Concentration in NiO Films To Enable in Situ PN Homojunctions. *ACS Applied Materials & Interfaces* **2019**, 11 (30), 27048-27056. https://doi.org/10.1021/acsami.9b04380
[26] Ghosh, S.; Mishra, S.; Singh, T. Antisolvents in Perovskite Solar Cells: Importance, Issues, and Alternatives. *Adv. Mater. Interfaces* **2020**, 7, 2000950. https://doi.org/10.1002/admi.202000950
[27] Babayigit, A.; D'Haen, J.; Boyen, H-G.; Conings, B. Gas Quenching for Perovskite Thin Film Deposition. *Joule* **2018**, 7 (2), 1205-1209. https://doi.org/10.1016/j.joule.2018.06.009
[28] Sánchez, S.; Jerónimo-Rendon, J.; Saliba, M.; Hagfeldt, A. Highly efficient and rapid manufactured perovskite solar cells via Flash InfraRed Annealing. *Materials Today* **2020**, 35, 9-15. https://doi.org/10.1016/j.mattod.2019.11.003
[29] Hilt, F.; Hovish, M. Q.; Rolston, N.; Bruning, K.; Tassone, C. J.; Dauskardt, R. H. Rapid route to efficient, scalable, and robust perovskite photovoltaics in air. *Energy Environ. Sci.* **2018**, 11, 2102-2113. https://doi.org/10.1039/C8EE01065J
[30] Mao, L.; Stoumpos C. C.; Kanatzidis, M. G. Two-Dimensional Hybrid Halide Perovskites: Principles and Promises. *J. Am. Chem. Soc.* **2019**, 141 (3), 1171-1190. https://doi.org/10.1021/jacs.8b10851
[31] Sala, J.; Heydarian, M.; Lammar, S.; Abdulraheem, Y.; Aernouts, T.; Hadipour, A.; Poortsmans, J. Compositional Investigation for Bandgap Engineering of Wide Bandgap Triple Cation Perovskite. *ACS Appl. Energy Mater.* **2021**, 4 (7), 6377-6384. https://doi.org/10.1021/acsaem.1c00810
[32] Wang, L.; Liu, G.; Xi, X.; Yang, G.; Hu, L.; Zhu, B.; He, Y.; Liu, Y.; Qian, H.; Zhang, S.; Zai, H. Annealing Engineering in the Growth of Perovskite Grains. *Crystals*. **2022**, 12 (7), 894. https://doi.org/10.3390/cryst12070894
[33] Suchan, K.; Just, J.; Becker, P.; Unger, E. L.; Unold, T. Optical in situ monitoring during the synthesis of halide perovskite solar cells reveals formation kinetics and evolution of optoelectronic properties. *J. Mater. Chem. A* **2020**, 8, 10439-10449. https://doi.org/10.1039/D0TA01237H

[34] Krückemeier, L.; Rau, U.; Stolterfoht, M.; Kirchartz, T.; How to Report Record Open-Circuit Voltages in Lead-Halide Perovskite Solar Cells. *Adv. Energy Mater.* **2020**, 1 (10), 1614-6832. https://doi.org/10.1002/aenm.201902573
[35] Habisreutinger, S. N.; Noel, N. K.; Snaith, H. J. Hysteresis Index: A Figure without Merit for Quantifying Hysteresis in Perovskite Solar Cells. *ACS Energy Lett.* **2018**, 3, 10, 2472–2476. https://doi.org/10.1021/acsenergylett.8b01627
[36] Zheng, X.; Hou, Y.; Bao, C.; Yin, J.; Yuan, F.; Huang, Z.; Song, K.; Liu, J.; Troughton, J.; Gasparini, N.; Zhou, C.; Lin, Y.; Xue, D-J.; Chen, B.; Johnston, A. K.; Wei, N.; Hedhili, M. N.; Wei, M.; Alsalloum, A. Y.; Maity, P.; Turedi, B.; Yang, C.; Baran, D.; Anthopoulos, T. D.; Han, Y.; Lu, Z-H.; Mohammed, O. F.; Gao, F.; Sargent, E. H.; Bakr, O. M. Managing grains and interfaces via ligand anchoring enables 22.3%-efficiency inverted perovskite solar cells. *Nat Energy* **2020**, 5, 131–140. https://doi.org/10.1038/s41560-019-0538-4
[37] Schindelin, J., Arganda-Carreras, I., Frise, E.; Kaynig, V.; Longair, M.; Pietzsch, T.; Preibisch, S.; Rueden, C.; Saalfeld, S.; Schmid, B.; Tinevez, J-Y.; White, D. J.; Hartenstein, V.; Eliceiri, K.; Tomancak, P.; Cardona, A. Fiji: an open-source platform for biological-image analysis. *Nat Methods* **2012**, 9, 676–682. https://doi.org/10.1038/nmeth.2019
[38] Rahmany, S.; Etgar, L. Semitrasnparent Perovskite Solar Cells. *ACS Energy Lett.* **2020**, 5 (5), 1519-1531. https://doi.org/10.1021/acsenergylett.0c00417